

# **Automated Detection of Left Ventricle in Arterial Input Function Images for Inline Perfusion Mapping using Deep Learning: A study of 15,000 Patients**

**Hui Xue<sup>1</sup>, Ethan Tseng<sup>1</sup>, Kristopher D Knott<sup>2</sup>, Tushar Kotecha<sup>3</sup>, Louise Brown<sup>4</sup>, Sven Plein<sup>4</sup>, Marianna Fontana<sup>3</sup>, James C Moon<sup>2</sup>, Peter Kellman<sup>1</sup>**

1. National Heart, Lung and Blood Institute, National Institutes of Health, Bethesda, MD, USA
2. Barts Heart Centre, London, UK
3. National Amyloidosis Centre, Royal Free Hospital, London, UK
4. Department of Biomedical Imaging Science, Leeds Institute of Cardiovascular and Metabolic Medicine, University of Leeds, Leeds, UK

## **Corresponding author:**

Hui Xue

Submit to Magnetic Resonance in Medicine

National Heart, Lung and Blood Institute  
National Institutes of Health  
10 Center Drive, Bethesda  
MD 20892  
USA

Phone: +1 (301) 827-0156

Cell: +1 (609) 712-3398

Fax: +1 (301) 496-2389

Email: [hui.xue@nih.gov](mailto:hui.xue@nih.gov)

**Word Count: 3,559**

[hui.xue@nih.gov](mailto:hui.xue@nih.gov)

[ethan.tseng@yahoo.com](mailto:ethan.tseng@yahoo.com)

[kristopher.knott@nhs.net](mailto:kristopher.knott@nhs.net)

[tushar.kotecha@nhs.net](mailto:tushar.kotecha@nhs.net)

[L.Brown1@leeds.ac.uk](mailto:L.Brown1@leeds.ac.uk)

[S.Plein@leeds.ac.uk](mailto:S.Plein@leeds.ac.uk)

[m.fontana@ucl.ac.uk](mailto:m.fontana@ucl.ac.uk)

[james@moonmail.co.uk](mailto:james@moonmail.co.uk)

[kellmanp@nhlbi.nih.gov](mailto:kellmanp@nhlbi.nih.gov)

## **Abstract**

### **Purpose**

Quantification of myocardial perfusion has the potential to improve detection of regional and global flow reduction. Significant effort has been made to automate the workflow, where one essential step is the arterial input function (AIF) extraction. Since failure here invalidates quantification, high accuracy is required. For this purpose, this study presents a robust AIF detection method using the convolutional neural net (CNN) model.

### **Methods**

CNN models were trained by assembling 25,027 scans (N=12,984 patients) from three hospitals, seven scanners. A test set of 5,721 scans (N=2,805 patients) evaluated model performance. The 2D+T AIF time series was inputted into CNN. Two variations were investigated: a) Two Classes (2CS) for background and foreground (LV mask); b) Three Classes (3CS) for background, foreground LV and RV. Final model was deployed on MR scanners via the Gadgetron.

### **Results**

Model loading time on MR scanner was ~340ms and applying it took ~180ms. The 3CS model successfully detect LV for 99.98% of all test cases (1 failed out of 5,721 cases). The mean Dice ratio for 3CS was  $0.87 \pm 0.08$  with 92.0% of all test cases having Dice ratio  $> 0.75$ , while the 2CS model gave lower Dice of  $0.82 \pm 0.22$  ( $P < 1e-5$ ). Extracted AIF signals using CNN were further compared to manual ground-truth for foot-time, peak-time, first-pass duration, peak value and area-under-curve. No significant differences were found for all features ( $P > 0.2$ ).

### **Conclusions**

This study proposed, validated, and deployed a robust CNN solution to detect the LV for the extraction of the AIF signal used in fully automated perfusion flow mapping.

**Key words**

Myocardial perfusion, Deep Learning, Arterial Input Function, Perfusion quantification, Inline AI, Gadgetron

## Introduction

Quantification of myocardial perfusion using dynamic cardiovascular magnetic resonance had been studied for over 20 years (1–7). Perfusion quantification is objective and shows potential to improve disease detection involving global flow reduction such as balanced multi-vessel coronary stenosis or microvascular dysfunction (8,9) and has prognostic value (10).

Significant effort has been made to automate the workflow of perfusion quantification, including imaging sequences (11,12), AIF signal correction (13–16), motion correction (17–20), and sector or pixel-wise flow estimation using either deconvolution (2,4,21) or tissue kinetics model (5,22–25). Deconvolution methods are based on the assumption of sufficient contrast agent extraction to the interstitium, while tissue kinetics modeling methods are more comprehensive to describe contrast dynamics during bolus injection (26,27).

One automated perfusion quantification system (28) was developed by our group. This solution utilized a "dual-sequence" perfusion imaging scheme with the dual-echo AIF T2\* signal loss correction. Perfusion images were acquired during free-breathing and automated motion correction was applied to align the myocardium over multiple heart beats, which enabled pixel-wise flow mapping. Since the accuracy of perfusion quantification highly depends on the correct measurement of the input contrast concentration, the "dual-sequence" imaging method acquired AIF images with low spatial resolution, very short saturation time and echo time, reducing signal saturation caused by high contrast concentration in blood.

Automated extraction of the AIF signal during contrast bolus passage is a prerequisite for automated perfusion quantification (Figure 1). An "ad-hoc" algorithm was previously proposed in (28) to detect a binary mask of the left ventricle from AIF image series. This algorithm was based on simple thresholding to mask off background and non-enhanced tissues

within the field-of-view (FOV) using signal up-slope. Resulting pixels were classified as left and right ventricle via k-means clustering. The AIF signal was computed by keeping pixels with high peak intensity to minimize partial-volume effects. While this method worked well during our initial testing (28), a higher failure rate (defined by mis-detecting the LV) was revealed after application to larger numbers of clinical adenosine stress studies. This occurred especially for patients with reduced or delayed AIF contrast concentration, possibly due to low cardiac output or incomplete contrast injection. Another reported method (29) to automatically detect AIF LV was based on thresholding the standard deviation map of time series, followed by LV pixel masking using independent component analysis. The AIF mask was also eroded to select high intensity pixels for time-intensity curve. While both algorithms utilized the contrast uptake dynamics of the LV, they were ad-hoc in the sense that manually crafted features (e.g. standard deviation or upslope maps) were designed as key algorithmic components, together with inflexible thresholding or clustering. Alternatively, a deep learning based solution has the potential to overcome these limitations by learning what is important for detecting the LV without potentially brittle “feature engineering” (30).

Failed detection of the AIF LV will result in an incorrect flow mapping. High accuracy is required for an automated solution. For this purpose, this study proposed an AIF LV detection method using deep learning. A convolutional neural net model was trained by assembling a very large data cohort from three hospitals. The 2D+T temporal AIF image series was inputted into NNs. A total of 25,027 scans comprised of both stress and rest scans from N=12,984 patients were collected for training. To test the trained model, an independent hold-out test set was collected, including 5,721 perfusion scans from N=2,805 patients. After training and evaluation, the final CNN model was integrated into the automated perfusion mapping software

that was deployed on the MR scanner via the Gadgetron InlineAI (31) software framework. The pre-trained CNN model was applied to the incoming AIF image series and outputted LV mask.

## **Methods**

### *Imaging and data collection*

Three hospitals participated in this study (Barts Heart Centre, Barts; Royal Free Hospital, RFH; Leeds Teaching Hospitals NHS Trust, LTHT). A total of 7 MR scanners were used. Five scanners were at Barts Heart Centre and affiliated Chenies Mews Imaging Center, including three 1.5T MAGNETOM Area and two MAGNETOM Prisma, Siemens AG Healthcare, Erlangen, Germany. A 1.5T MAGNETOM Area was used at the Royal Free Hospital and LTHT had a MAGNETOM Prisma 3T scanner.

Adenosine stress and rest perfusion imaging were performed at participating sites using the "dual-sequence" scheme (5). This imaging sequence utilized saturation recovery and single-shot readout. Three short axis slices were imaged for 60 heart beats after injection of the contrast bolus. An AIF imaging module was inserted before the perfusion imaging and played out after the R wave trigger with very short delay. AIF images were acquired at the most basal slice. Imaging parameters for AIF were: FOV 360×270 mm<sup>2</sup>, slice thickness 10 mm, small imaging matrix 64×48 (linear order), interleaved acceleration R=3, two echo readouts, TE=0.76 and 1.76ms, TR=2.45ms, short trigger delay TD=4.2ms, imaging duration 42ms, flip angle 5°, FLASH readout, total duration including SR preparation was 57ms. The same imaging sequence was used in all hospitals for all patients.

Data were acquired with the required ethical and/or audit secondary use approvals or guidelines (as per each center) that permitted retrospective analysis of anonymized data for the purpose of technical development, protocol optimization and quality control. All data were

anonymized and de-linked for analysis by NIH with approval by the NIH Office of Human Subjects Research OHSR (Exemption #13156). A total of 25,027 scans (10,349 stress) were retrospectively included for training the model, which counted for N=12,984 consecutive patients at three sites (941 patients had only rest perfusion). This data cohort was acquired from 29 April 2016 to 15 February 2019. To test the AIF detection, a separate test set was assembled retrospectively. Imaging for the test set was from 16 February 2019 to 13 August 2019. This cohort consists of N=2,805 patients and 5,721 perfusion scans (2,780 stress).

### *Neural Net model*

The AIF image series was first temporally resampled to be on a 0.5s grid (5,28), to account for heart rate variation or any missed ECG triggers during image acquisition. The first 64 saturation recovery images (initial proton density images are excluded) after temporal resampling were selected, resulting in an image array of 64×48×64. This image array was used for training and testing. Figure 1 gives an example of an AIF image series (first 48 saturation recovery images) after resampling and the corresponding LV mask manually established.

The U-net semantic segmentation architecture (32,33) was modified for the AIF LV detection. As shown in Figure 2, a ResNet module (34) was used as the basic building block, which consisted of: batch normalization (BN), rectified linear unit (Relu), and convolution (CONV) components as shown. To simplify the neural net specification, one module consists of two convolution layers with the same number of filter outputs. As shown in Figure 2, the downsampling and upsampling branches were connected by "skip-connections". The AIF times series went through the input layer followed by the downsampling branch. As the spatial resolution was reduced, the number of filters increased. The upsampling branch increased the spatial resolution and reduced the number of filters. Final CONV layer outputted a 64×48×C

array for segmented classes C. The output of the NN was inputted into a pixel-wise sigmoid or softmax layer to estimate probability maps. Final segmentation masks were derived by thresholding the probability maps. All CONV layers used a 3x3 kernel with stride 1 and padding 1.

The loss function was a weighted sum of cross-entropy loss and the Intersection Over Union (so-called IoU or Jaccard index). For the binary mask  $y^i$  and predicted probability  $\hat{y}^i$ , the IoU was computed as :

$$J_{IoU} = \frac{1}{N} \sum_{i=0}^{N-1} \frac{y^i \hat{y}^i}{y^i + \hat{y}^i - y^i \hat{y}^i} \quad (1)$$

where N is the number of pixels and  $i$  is the index of pixels. The total cost was the weighted sum (35):

$$J = J_{cross-entropy} - 0.5 \cdot \log(J_{IoU}) \quad (2)$$

This cost function simultaneously maximizes the probability that a pixel is correctly classified and optimizes the overlap between detected mask and ground-truth. This scheme demonstrated improved segmentation accuracy in past MICCAI segmentation challenge (36).

Each AIF dataset was corrected for spatial variation in receive coil sensitivities using the proton density (PD) weighted images acquired at the start of acquisition, and were scaled to have the greatest value be 1 before inputting for training or testing:  $AIF = AIF / \max(AIF)$ . Random flipping along readout and phase directions (probability to apply flipping was 0.5) was used as a data augmentation step before training.

### ***Bootstrap data labelling***

Given the large number of datasets, a bootstrap strategy was implemented to speed up data labelling. First, the respiratory motion was corrected from AIF image series using a motion



correction algorithm designed for free-breathing cardiac perfusion (5,28). The corrected images series were inputted for LV labelling using the "ad-hoc" algorithm previously proposed (5,28). In this method, the noise background was removed using a simple thresholding with  $SNR < 3$ . LV was detected by clustering the temporal intensity curves. This heuristic algorithm was applied to all samples. All results were visually inspected to either accept or correct tentative labels (H.X., with 9 years of experiences in perfusion imaging). Failed cases were manually corrected and included in the training set. Approx. 200 hours were spent on labelling the entire data cohort.

### ***LV detection utilizing 2D+T contrast dynamics***

With the motion corrected AIF series, a 2D+T temporal image array was assembled and inputted into the NN. To train the NN with more input features, the right ventricle was further marked as another object class. The motivation was to utilize the unique contrast update dynamics and consistent anatomy between the LV and RV, as the RV was first enhanced before arrival of contrast in LV. Two variations of NNs were investigated: a) Two Classes (2CS) for background and foreground (LV mask); b) Three Classes (3CS) for background, foreground LV and foreground RV regions. The hypothesis was that the extra information on RV contrast dynamics may lead to improved LV detection.

### ***Training and hyperparameter search***

The training data were randomly shuffled and split into training set (Tra) (number of scans,  $N=22,941$ ) and development set (Dev,  $N=2,086$ ). Both Tra and Dev sets were processed with the initial heuristic method and visually inspected for success/failure and manually corrected to derive the labeled set. Figure 3 illustrates AIF image variation on anatomy and imaging.

Furthermore, there is considerable variation of the AIF temporal response, both bolus arrival time and duration. The NN model was implemented using PyTorch (37) and training was performed on an Ubuntu 18.04 PC with four NVIDIA GTX 2080Ti GPU cards, each with 11GB RAM. In initial experiments, it was determined that number of ResNet modules and number of CONV filters in the NN had the most significant impact on the detection accuracy. Therefore, a hyperparameter search was conducted to test different combinations (5 to 9 ResNet modules, number of CONV filters from 64 to 256). For all tests, the Adam optimizer was used with initial learning rate being 0.001. The betas were 0.9 and 0.999. Epsilon was  $1e-8$ . Learning rate was reduced by x2 for every 10 epochs. Training took 40 epochs and the best model was selected as the one giving best performance on the Dev set.

### *Analysis*

The success of LV detection was initially quantified by Dice ratio (38). Following convention often used in deep learning based object detection and semantic segmentation (39,40), if the Dice ratio between ground-truth mask and NN result was greater than 0.5, the detection was defined as being successful. The Dice ratio over 0.75 was also reported as the second.

The detected AIF signal curve was further compared to the corresponding ground-truth. AIF foot time, peak time, peak value, first-pass duration (from foot to valley, as illustrated in Figure 1), area-under-curve (AUC) for first pass and correlation coefficient (CC) were computed for both auto and manual curves. Since dual sequence has a low spatial resolution for AIF images, edge pixels of the AIF LV can often have reduced intensity values due to partial volume with adjacent tissue. The LV mask was further eroded to keep the top 15% percentile values for computing the time-intensity curves, as in previous studies (28).

The resulting values were presented as mean +/- standard deviation. A t-test was performed and a P-value less than 0.05 was considered statistically significant.

### ***Inline integration***

The training of NN models were conducted offline using Pytorch. The resulting models were integrated inline to run on MR scanners. The inline integration was achieved using the Gadgetron Inline AI (31). The key components were a set of interfaces to load pre-saved NN models and apply the model on incoming data (so-called "inference"). This involved the transfer of model objects from Pytorch to C++ and passing data from C++ to Pytorch modules. Since Gadgetron may run with different computing configurations, such as on the scanner image reconstruction computer, on a user supplied computing server, or on cloud nodes (41,42), the model inference step was chosen to run without GPU. That is, the inference was performed on CPU. While training can be prohibitively slow with only CPU, our tests showed CPU inference for AIF detection took sub-seconds for clinical perfusion scans.

The NN based AIF detection was integrated into inline perfusion flow mapping workflow. The model loading was performed as soon as the imaging sequence was initialized. The loaded model was kept in the Gadgetron runtime environment and applied to the incoming AIF image array. The resulting LV mask and AIF signal was used for downstream perfusion quantification. Thus, using the Gadgetron streaming framework with the Inline AI infrastructure, an AIF detection scheme powered by deep learning was achieved on clinical MR scanners.

## Results

A training session took ~40 mins for 40 epochs. Figure 4a gives the cost vs. the number of iterations in training. The Adam optimizer used in the training was very efficient to drive down the total cost and increase detection accuracy. A total of 45 training sessions was performed for the hyperparameter search, which took ~32 hours. After hyperparameter search, best performance was achieved for the architecture consisting of 8 ResNet modules and 128 CONV filters. These parameters were selected for all following performance measurement.

The three-class segmentation outperformed two-class segmentation. The 3CS model successfully detected the LV for 99.98% of all test set cases (1 failed out of 5,721 cases), while original ad-hoc detection had 52 failed cases. The mean Dice ratios for 3CS and 2CS were  $0.87 \pm 0.08$  and  $0.82 \pm 0.22$  ( $P < 1e-5$ ). Figure 4b gives the histogram of three-class detection for all test cases, showing 92.0% of all test cases had a Dice ratio higher than 0.75. As a comparison, the two-class detection had 80.8% cases with Dice ratio higher than 0.75.

Figure 5 gives examples of AIF detection with different Dice ratios from the Test set, to illustrate detection performance for different levels of accuracy. Those cases with lower Dice still located the LV blood pool successfully.

Foot and peak time for labelled data were  $14.0 \pm 3.41s$  and  $18.0 \pm 4.52s$ , compared to three-class NN of  $14.0 \pm 3.42s$  and  $18.0 \pm 4.55s$ . First-pass duration was  $13.2 \pm 4.97s$  and  $13.2 \pm 5.00s$  for label and NN, respectively. Normalized intensity values at peak were  $0.385 \pm 0.099$  for label and  $0.383 \pm 0.099$  for NN. AUC was  $6.14 \pm 2.18$  for label and  $6.12 \pm 2.19$  for NN. No significant differences were found for all results ( $P > 0.2$ ). CC was  $0.998 \pm 0.012$ . Figure 6 gives the Bland-Altman plots of NN results vs. label masking.

The NN model was integrated and tested on all MR scanners as a component of inline perfusion mapping. The reconstruction workflow was configured so that Gadgetron server started to load the saved model while a perfusion sequence was under preparation on the scanner. Model loading time was ~340ms and applying the model on an incoming AIF image array was ~180ms. These timing results were measured with CPU inference (2× Intel Xeon Gold 6152 CPU, 2.10GHz, 192GB RAM).

## **Discussion**

Reliability is paramount for in-line mapping solutions since they must be fully automatic. The proposed CNN based solution greatly improved on the prior method by approximately 50:1, decreasing the failure rate from 0.9% to less than 0.02%.

While no prior study has reported on the application of a convolutional neural net for perfusion AIF LV detection, pixel-wise image segmentation using NN has been well studied. The first well-known algorithm is the fully convolutional network (FCN) (43), which repurposed classification networks for pixel-wise segmentation by modifying the output layer and loss function. Extensions of these networks include adding encoding-decoding structures and expanding the filter depth while reducing the spatial resolution (32,44–46). These NNs added skip connections between corresponding down/upsampling layers, to allow detailed pixel-level segmentation. This led to major improvement in performance, as demonstrated by U-net (32) and Seg-net (45). The U-net architecture was further extended by using recurrent (47) and residual modules (48). More recent variations include V-net (44) and TerausNet (35), which kept the skip connections, but had different number of convolution filters and kernel size in each down/upsampling layer. These segmentation NNs have been used for cardiac MR image segmentation. The first well-known work utilized a modified FCN network to segment

myocardium from cine imaging (49). Recent published work includes automated analysis of T1 mapping image (50) and cardiac flow images (51).

The proposed approach utilized a 2D+T AIF image series as input to the NNs, different from Cine deep learning segmentation using individual 2D images (49). Since perfusion images show significant contrast variation during bolus passage, inputting the temporal image series allowed NNs to utilize the full bolus passage information for LV detection. As a pre-processing step, motion correction was applied to AIF image series to correct the respiratory motion from free-breathing imaging. This step allowed a single LV mask to be detected. It also simplified the neural net architecture for LV detection, because omitting MOCO will force NNs to produce a mask for every AIF image.

Experimental results showed that the neural net with three-class training set (3CS) outperformed two-class detection (2CS). This result demonstrated the added value of extra labelling on the given AIF time series. By providing the context information of the RV, the NNs learned the relative LV anatomy better. The contrast enhancement pattern of the RV, which reaches peak contrast sooner than the LV, is a useful prior for NNs to capture. Similar performance boosting by combining additional prior information has previously been described in other applications, such as multi-organ segmentation using CNN (52).

One major barrier for more detailed labelling in deep learning is establishing large training sets, which come with the need for both expert hours and high financial costs. The computer vision community generates gigantic datasets of labelled images by hiring "common" workers through the internet (e.g. "crowdsourcing" in Amazon Market Place), such as in ImageNet (53) and Microsoft COCO (54). However, this strategy may not be feasible for medical imaging, due to required professional knowledge and expertise. While some methods

such as MOCO or the bootstrap strategy used in this study may be helpful to speed up the labelling process, developers of cardiac deep learning applications still spend significant hours establishing training sets (55). Recent development of synthetic data labelling can learn a generative model from a small training set and synthesize more training data by sampling the learned probability distribution (56). This strategy is promising with the need of expert supervision to verify the generated labels are correct. Another related method to mitigate data labelling workload is through transfer learning. As an example, large cardiac cine datasets labelled by experts do exist (e.g. UK biobank data used in (49)). Since early layers of NNs often learn similar low-level features, it is possible to use cine model weights of early layers for another application. In this way less new data may be required.

This study presented a CNN based solution for AIF LV detection and the inline integration of models on MR scanners through the Gadgetron InlineAI (31). Although NN training is known to be computationally heavy, we showed that model inference is fast through CPU on the MR scanner. As a result, applying deep learning for advanced cardiac MR is becoming practical in the clinical setting and this study serves as a new example of this type.

## **Conclusions**

This study validated and deployed a CNN based solution to detect the LV blood pool from an arterial input function image series, as a prerequisite step for perfusion flow mapping. A large training set of 25,027 perfusion scans was retrospectively analyzed from three hospitals to train the NN models. Testing was performed on a separate set of 5,721 scans, giving a high LV detection rate of 99.98% and mean Dice ratio of  $0.87 \pm 0.08$ .

## Abbreviations

AIF	arterial input function
AUC	area-under-curve
DSC	Dice similarity coefficient
FA	flip angle
FLASH	fast low angle shot
FOV	field-of-view
IoU	Intersection over Union
MBF	myocardial blood flow
MOCO	motion correction
NN	neural network
PD	proton density
SNR	signal-to-noise ratio
SR	saturation recovery
SSFP	steady state free precession
TD	saturation recovery delay time
TS	saturation time



## **Declarations**

### **Ethical Approval and Consent to participate**

Data was acquired with the required ethical and/or audit secondary use approvals or guidelines (as per each center) that permitted retrospective analysis of anonymized data for the purpose of technical development and protocol optimization and quality control. All data was anonymized and de-linked for analysis by NIH with approval by the NIH Office of Human Subjects Research OHSR (Exemption #13156).

### **Consent for publication**

Data was acquired with the required ethical and/or audit secondary use approvals or guidelines (as per each center) that permitted retrospective analysis of anonymized data and publication. The per center IRB approval document is available for review by the Editor-in-Chief.

### **Availability of data and material**

The raw data that support the findings of this study are available from the corresponding author upon reasonable request subject to restriction on use by the Office of Human Subjects Research. The source file to train the CNN model is available at <https://github.com/xueh2/QPerf.git>. Example datasets were provided at this website with user guide to run pre-trained models for LV detection.

### **Competing interests**

The authors declare that they have no competing interests

## **Funding**

Supported by the National Heart, Lung and Blood Institute, National Institutes of Health by the Division of Intramural Research and the British Heart Foundation (CH/16/2/32089).

### **Authors' contributions**

HX and PK conceived of the study and drafted the manuscript. HX, PK and ET developed the algorithms, implemented the inline integration of neural net model and performed processing and analysis. KK, TK, LB, SP, MF, JM were responsible for CMR studies used in training and test. All authors participated in revising the manuscript and read and approved the final manuscript.

## References

1. Zierler K. Indicator dilution methods for measuring blood flow, volume, and other properties of biological systems: a brief history and memoir. *Ann. Biomed. Eng.* 2000;28:836–848 doi: 10.1114/1.1308496.
2. Jerosch-Herold M, Stillman a E, Wilke N. Magnetic resonance quantification of the myocardial perfusion reserve with a Fermi function model for constrained deconvolution. *Med. Phys.* 1998;25:73–84 doi: 10.1118/1.598163.
3. Tofts PS. Modeling tracer kinetics in dynamic Gd-DTPA MR imaging. *J. Magn. Reson. Imaging* 1997;7:91–101 doi: 10.1002/jmri.1880070113.
4. Larsson HB, Fritz-Hansen T, Rostrup E, Søndergaard L, Ring P, Henriksen O. Myocardial perfusion modeling using MRI. *Magn. Reson. Med.* 1996;35:716–726 doi: 10.1002/mrm.1910350513.
5. Kellman P, Hansen MS, Nielles-Vallespin S, et al. Myocardial perfusion cardiovascular magnetic resonance: optimized dual sequence and reconstruction for quantification. *J. Cardiovasc. Magn. Reson.* 2017;19:43 doi: 10.1186/s12968-017-0355-5.
6. Hsu LY, Groves DW, Aletras AH, Kellman P, Arai AE. A quantitative pixel-wise measurement of myocardial blood flow by contrast-enhanced first-pass CMR perfusion imaging: Microsphere validation in dogs and feasibility study in humans. *JACC Cardiovasc. Imaging* 2012;5:154–166 doi: 10.1016/j.jcmg.2011.07.013.
7. Chiribiri A, Schuster A, Ishida M, et al. Perfusion phantom: An efficient and reproducible method to simulate myocardial first-pass perfusion measurements with cardiovascular magnetic resonance. *Magn. Reson. Med.* 2013;69:698–707 doi: 10.1002/mrm.24299.
8. Schindler TH, Schelbert HR, Quercioli A, Dilsizian V. Cardiac PET imaging for the detection and monitoring of coronary artery disease and microvascular health. *JACC Cardiovasc. Imaging* 2010;3:623–640 doi: 10.1016/j.jcmg.2010.04.007.
9. Zorach B, Shaw PW, Bourque J, et al. Quantitative cardiovascular magnetic resonance perfusion imaging identifies reduced flow reserve in microvascular coronary artery disease. *J. Cardiovasc. Magn. Reson.* 2018;20:1–8 doi: 10.1186/s12968-018-0435-1.
10. Sammut EC, Villa ADM, Di Giovine G, et al. Prognostic Value of Quantitative Stress Perfusion Cardiac Magnetic Resonance. *JACC Cardiovasc. Imaging* 2018;11:686–694 doi: 10.1016/j.jcmg.2017.07.022.
11. Fair MJ, Gatehouse PD, DiBella EVR, Firmin DN. A review of 3D first-pass, whole-

heart, myocardial perfusion cardiovascular magnetic resonance. *J. Cardiovasc. Magn. Reson.* 2015;17:68 doi: 10.1186/s12968-015-0162-9.

12. Kellman P, Arai AE. Imaging sequences for first pass perfusion --a review. *J. Cardiovasc. Magn. Reson.* 2007;9:525–537 doi: 10.1080/10976640601187604.

13. Gatehouse PD, Elkinington AG, Ablitt N a, Yang G-Z, Pennell DJ, Firmin DN. Accurate assessment of the arterial input function during high-dose myocardial perfusion cardiovascular magnetic resonance. *J. Magn. Reson. Imaging* 2004;20:39–45 doi: 10.1002/jmri.20054.

14. Kellman P, Aletras AH, Hsu LY, McVeigh ER, Arai AE. T2\* measurement during first-pass contrast-enhanced cardiac perfusion imaging. *Magn. Reson. Med.* 2006;56:1132–1134 doi: 10.1002/mrm.21061.

15. Cernicanu A, Axel L. Theory-Based Signal Calibration with Single-Point T1 Measurements for First-Pass Quantitative Perfusion MRI Studies. *Acad. Radiol.* 2006;13:686–693 doi: 10.1016/j.acra.2006.02.040.

16. Christian TF, Rettmann DW, Aletras AH, et al. Absolute myocardial perfusion in canines measured by using dual-bolus first-pass MR imaging. *Radiology* 2004;232:677–684 doi: 10.1148/radiol.2323030573.

17. Yang GZ, Burger P, Panting J, et al. Motion and deformation tracking for short-axis echo-planar myocardial perfusion imaging. *Med. Image Anal.* 1998;2:285–302 doi: 10.1016/S1361-8415(98)80024-8.

18. Milles J, Geest RJ Van Der, Jerosch-Herold M, Reiber J, Lelieveldt B. Fully Automated Motion Correction in First-Pass Myocardial Perfusion MR Image Sequences. *IEEE Trans. Med. Imaging* 2008;27:1611–1621 doi: 10.1109/TMI.2008.928918.

19. Pontre B, Cowan BR, DiBella E, et al. An Open Benchmark Challenge for Motion Correction of Myocardial Perfusion MRI. *IEEE J. Biomed. Heal. Informatics* 2017;21:1315–1326 doi: 10.1109/JBHI.2016.2597145.

20. Scannell CM, Villa ADM, Lee J, Breeuwer M, Chiribiri A. Robust non-rigid motion compensation of free-breathing myocardial perfusion MRI data. *IEEE Trans. Med. Imaging* 2019 doi: 10.1109/tmi.2019.2897044.

21. Jerosch-Herold M, Wilke N, Stillman a E. Magnetic resonance quantification of the myocardial perfusion reserve with a Fermi function model for constrained deconvolution. *Med. Phys.* 1998;25:73–84 doi: 10.1118/1.598163.

22. Fluckiger JU, Benefield BC, Bakhos L, Harris KR, Lee DC. A Comparison of Theory-Based and Experimentally Determined Myocardial Signal Intensity Correction Methods in First-Pass Perfusion Magnetic Resonance Imaging. *Comput. Math. Methods Med.* 2015;9.
23. Bassingthwaighte JB, Sparks HVJ, Chan IS, Dewitt DF, Gorman MW. Modeling of transendothelial transport. *Fed Proc.* 1985;44:2623–2626 doi: 10.1016/j.micinf.2011.07.011.Innate.
24. Sourbron SP, Buckley DL. Tracer kinetic modelling in MRI: estimating perfusion and capillary permeability. *Phys. Med. Biol.* 2011;57:1–33 doi: 10.1088/0031-9155/57/2/R1.
25. Broadbent DA, Biglands JD, Larghat A, et al. Myocardial blood flow at rest and stress measured with dynamic contrast-enhanced MRI: Comparison of a distributed parameter model with a fermi function model. *Magn. Reson. Med.* 2013;70:1591–1597.
26. Bassingthwaighte JB, Sparks H V. Indicator dilution estimation of capillary endothelial transport. *Annu. Rev. Physiol.* 2013;18:1199–1216 doi: 10.1016/j.micinf.2011.07.011.Innate.
27. Koh TS, Response I. Tracer Kinetics Modeling Basics: Model Formulation. 2010;18:2–4.
28. Xue H, Brown LAE, Nielles-Vallespin S, Plein S, Kellmann P. Automatic In-line Quantitative Myocardial Perfusion Mapping : processing algorithm and implementation. *Magn. Reson. Med.* 2019 doi: 10.1002/mrm.27954.
29. Jacobs M, Benovoy M, Chang LC, Arai AE, Hsu LY. Evaluation of an automated method for arterial input function detection for first-pass myocardial perfusion cardiovascular magnetic resonance. *J. Cardiovasc. Magn. Reson.* 2016;18:1–11 doi: 10.1186/s12968-016-0239-0.
30. LeCun Y, Bengio Y, Hinton G, Y. L, Y. B, G. H. Deep learning. *Nature* 2015;521:436–444 doi: 10.1038/nature14539.
31. Xue H, Davies R, Hansen D, et al. Gadgetron Inline AI : Effective Model inference on MR scanner. In: *ISMRM.* ; 2019. p. 4837.
32. Ronneberger O, Fischer P, Brox T. U-net: Convolutional networks for biomedical image segmentation. *Lect. Notes Comput. Sci.* 2015;9351:234–241 doi: 10.1007/978-3-319-24574-4\_28.
33. Zhang Z, Liu Q, Wang Y. Road Extraction by Deep Residual U-Net. *IEEE Geosci. Remote Sens. Lett.* 2018:1–5 doi: 10.1109/LGRS.2018.2802944.

34. Xie S, Girshick R, Dollár P, Tu Z, He K. Aggregated residual transformations for deep neural networks. CVPR 2017:5987–5995 doi: 10.1109/CVPR.2017.634.
35. Shvets A, Rakhlin A, Kalinin AA, Iglovikov V. Automatic Instrument Segmentation in Robot-Assisted Surgery Using Deep Learning. 17th IEEE Int. Conf. Mach. Learn. Appl. 2018:624–628 doi: 10.1109/ICMLA.2018.00100.
36. Allan M, Shvets A, Kurmann T, et al. 2017 Robotic Instrument Segmentation Challenge. arXiv:1902.06426 [cs.CV] 2017:1–14.
37. Paszke A, Gross S, Chintala S, et al. Automatic differentiation in pytorch. In: 31st Conference on Neural Information Processing Systems. ; 2017. pp. 1–8. doi: 10.1145/24680.24681.
38. Dice LR. Measures of the Amount of Ecologic Association Between Species. Ecology 1945;26:297–302.
39. He K, Gkioxari G, Dollár P, Girshick R. Mask R-CNN. Proc. IEEE Int. Conf. Comput. Vis. 2017;2017-October:2980–2988 doi: 10.1109/ICCV.2017.322.
40. Redmon J, Farhadi A. YOLO9000: Better , stronger , faster. In: CVPR. ; 2017.
41. Hansen MS, Sørensen TS. Gadgetron: An open source framework for medical image reconstruction. Magn. Reson. Med. 2013;69:1768–1776 doi: 10.1002/mrm.24389.
42. Xue H, Inati S, Sørensen TS, Kellman P, Hansen MS. Distributed MRI reconstruction using gadgetron-based cloud computing. Magn. Reson. Med. 2015;73:1015–1025 doi: 10.1002/mrm.25213.
43. Long J, Shelhamer E, Darrell T. Fully convolutional networks for semantic segmentation. Proc. IEEE Comput. Soc. Conf. Comput. Vis. Pattern Recognit. 2015:3431–3440 doi: 10.1109/CVPR.2015.7298965.
44. Milletari F, Navab N, Ahmadi SA. V-Net: Fully convolutional neural networks for volumetric medical image segmentation. In: 4th International Conference on 3D Vision. ; 2016. pp. 565–571. doi: 10.1109/3DV.2016.79.
45. Badrinarayanan V, Kendall A, Cipolla R. SegNet: A Deep Convolutional Encoder-Decoder Architecture for Image Segmentation. IEEE Trans. Pattern Anal. Mach. Intell. 2017;39:2481–2495 doi: 10.1109/TPAMI.2016.2644615.
46. Kendall A, Badrinarayanan V, Cipolla R. Bayesian SegNet: Model Uncertainty in Deep

Convolutional Encoder-Decoder Architectures for Scene Understanding. In: The British Machine Vision Conference. ; 2017. doi: 10.13140/RG.2.1.2985.2407.

47. Alom MZ, Hasan M, Yakopcic C, Taha TM, Asari VK. Recurrent Residual Convolutional Neural Network based on U-Net (R2U-Net) for Medical Image Segmentation. arXiv:1802.06955 [cs.CV] 2018.

48. Girshick R, Donahue J, Darrell T, Malik J. Rich feature hierarchies for accurate object detection and semantic segmentation. Proc. IEEE Comput. Soc. Conf. Comput. Vis. Pattern Recognit. 2014:580–587 doi: 10.1109/CVPR.2014.81.

49. Bai W, Sinclair M, Tarroni G, et al. Automated cardiovascular magnetic resonance image analysis with fully convolutional networks. J. Cardiovasc. Magn. Reson. 2018;20.

50. Fahmy AS, El-Rewaidy H, Nezafat M, Nakamori S, Nezafat R. Automated analysis of cardiovascular magnetic resonance myocardial native T1 mapping images using fully convolutional neural networks. J. Cardiovasc. Magn. Reson. 2019;21:1–12 doi: 10.1186/s12968-018-0516-1.

51. Bratt A, Kim J, Pollie M, et al. Machine learning derived segmentation of phase velocity encoded cardiovascular magnetic resonance for fully automated aortic flow quantification. J. Cardiovasc. Magn. Reson. 2019;21:1–11 doi: 10.1186/s12968-018-0509-0.

52. Zhou Y, Li Z, Bai S, et al. Prior-aware Neural Network for Partially-Supervised Multi-Organ Segmentation. arXiv:1904.06346 [cs.CV] 2019

53. Li F, Li K, Berg A. ImageNet: crowdsourcing, benchmarking & other cool things. In: CMU VASC Seminar. 2010.

54. Lin TY, Maire M, Belongie S, et al. Microsoft COCO: Common objects in context. Lect. Notes Comput. Sci. 2014;8693:740–755 doi: 10.1007/978-3-319-10602-1\_48.

55. Langlotz CP, Allen B, Erickson BJ, et al. A Roadmap for Foundational Research on Artificial Intelligence in Medical Imaging: From the 2018 NIH/RSNA/ACR/The Academy Workshop. Radiology 2019:190613 doi: 10.1148/radiol.2019190613.

56. Kazemnia S, Baur C, Kuijper A, et al. GANs for Medical Image Analysis. arXiv:1809.06222 [cs.CV] 2018:1–41.



## List of Captions

**Figure 1** Example of AIF image series. (a) AIF 2D+T time series, demonstrating the passage of contrast bolus. (b) AIF image with LV mask overlaid. (c) AIF time intensity curve extracted from LV mask with the foot, peak and valley points indicated.

**Figure 2** ResUnet architecture used for AIF LV mask detection. The 2D+T AIF time series after motion correction is input to the CNN and passed through the downsample branch with gradually reduced spatial resolution. This process is reverted through the upsample branch until the original spatial resolution is restored. Skip-connections between down- and up-sample branches allows the neural net to learn detailed features at each spatial resolution. More ResNet modules can be inserted into the neural net to adjust its depth.

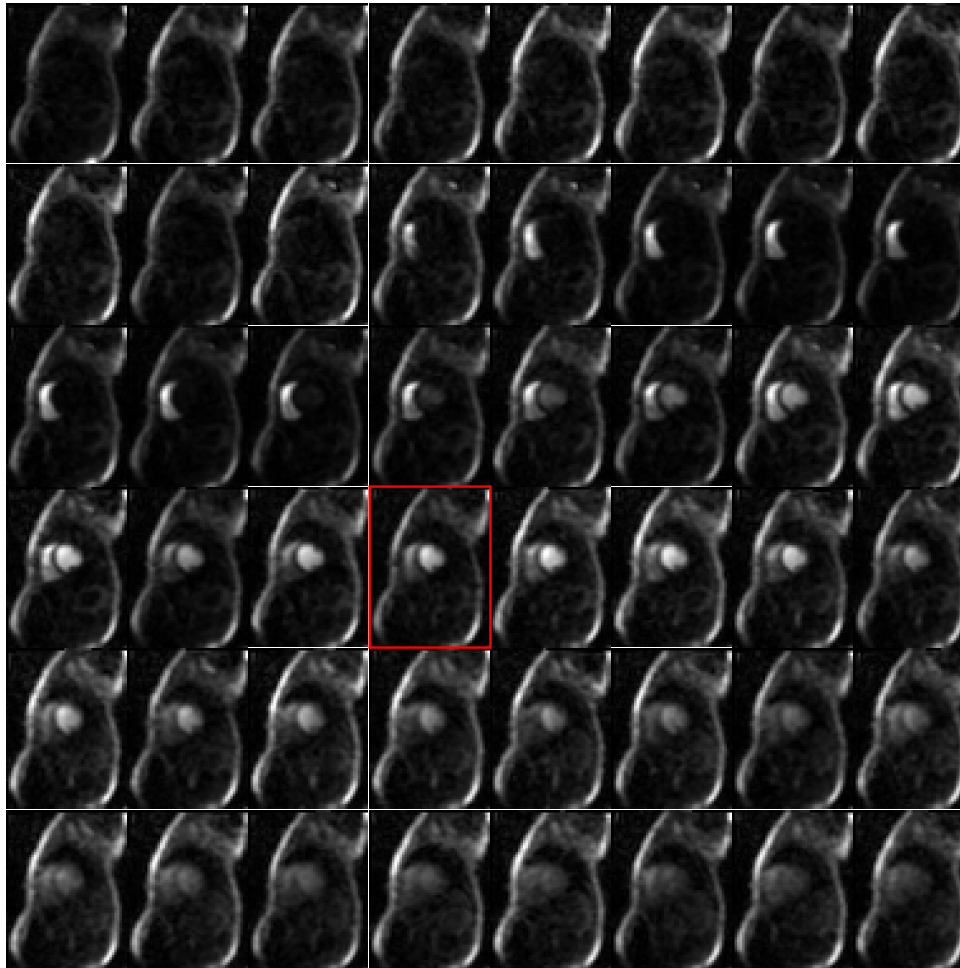
**Figure 3** Illustration of anatomical variation in the data cohort illustrating a range of variation in anatomy and imaging for which the detection algorithm must cope.

**Figure 4** AIF detection performance on the test set. (a) loss vs. the number of iterations for a typical training session, (b) histogram of three-class detection for all test cases, showing majority of cases have high dice scores.

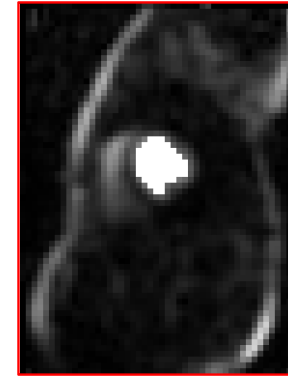
**Figure 5** Examples of AIF detection with different level of performance. Cases with lower score still located the LV blood pool successfully.

**Figure 6** Bland Altman plots for parameters derived from AIF signal curve comparing manually labelled vs. CNN.

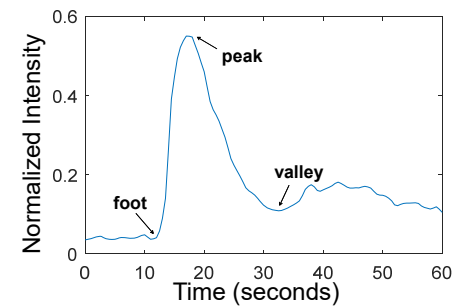
**Figure 1** Example of AIF image series. (a) AIF 2D+T time series, demonstrating the passage of contrast bolus. (b) AIF image with LV mask overlaid. (c) AIF time intensity curve extracted from LV mask with the foot, peak and valley points indicated.



(a) An example of AIF image series



(b) An AIF image with LV mask overlay.



(c) AIF time intensity curve extracted from LV mask

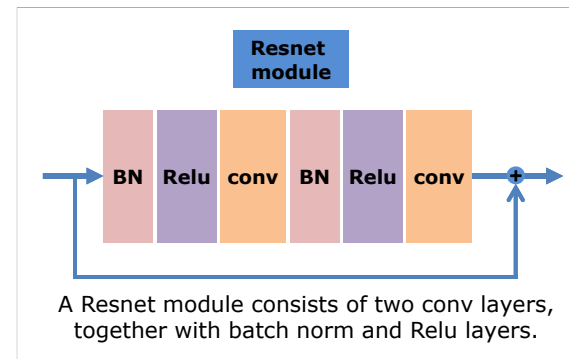
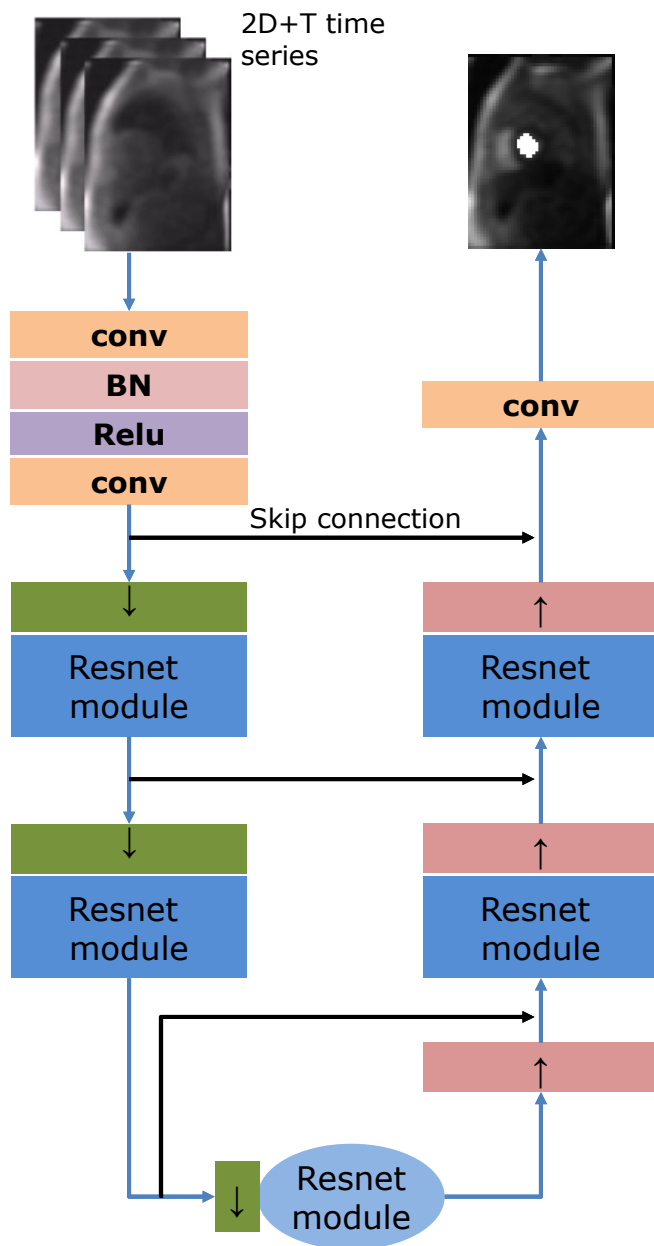


**Figure 2** ResUnet architecture used for AIF LV mask detection. . The 2D+T AIF time series after motion correction is input to the CNN and passed through the downsample branch where the spatial resolution is halved with each unit. This process is reverted through the upsample branch until the original spatial resolution is restored. Skip-connections are established between down- and upsample branches to allow neural net to be adaptively learn through spatial resolution. More resnet modules can be inserted into the neural net to adjust its depth.

**Figure 3** Illustration of anatomical variation in the data cohort illustrating a range of variation in anatomy and imaging for which the detection algorithm must cope.

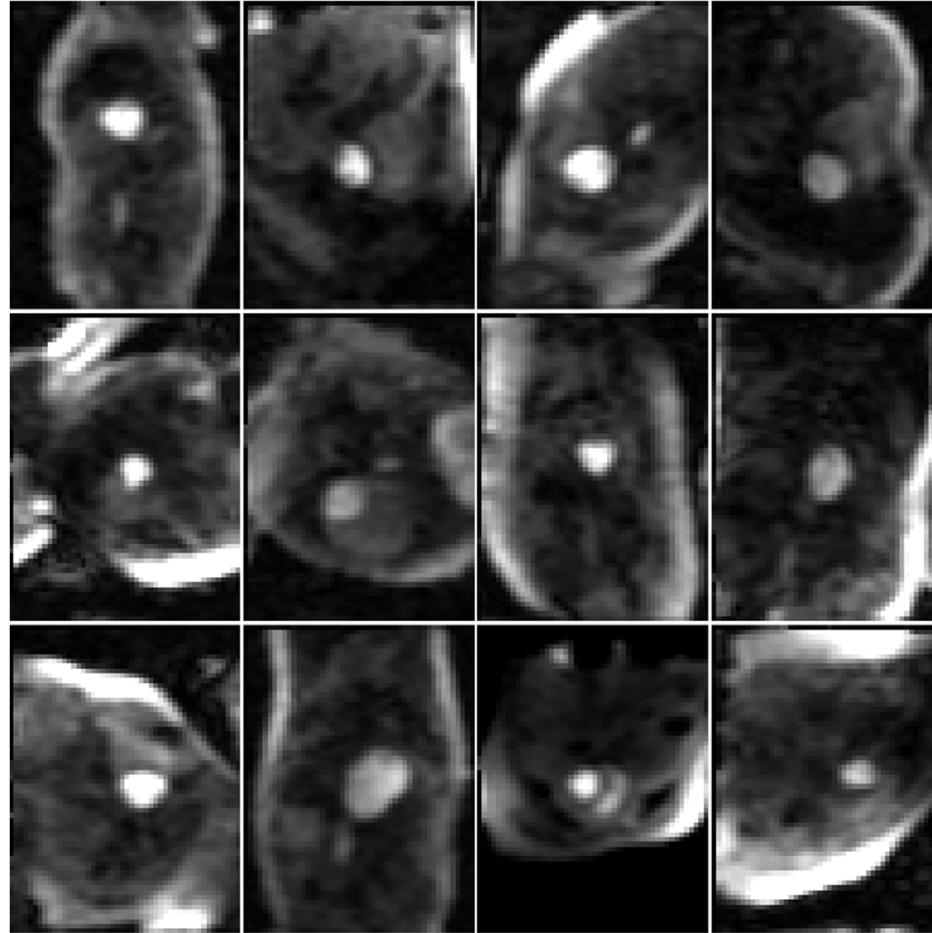
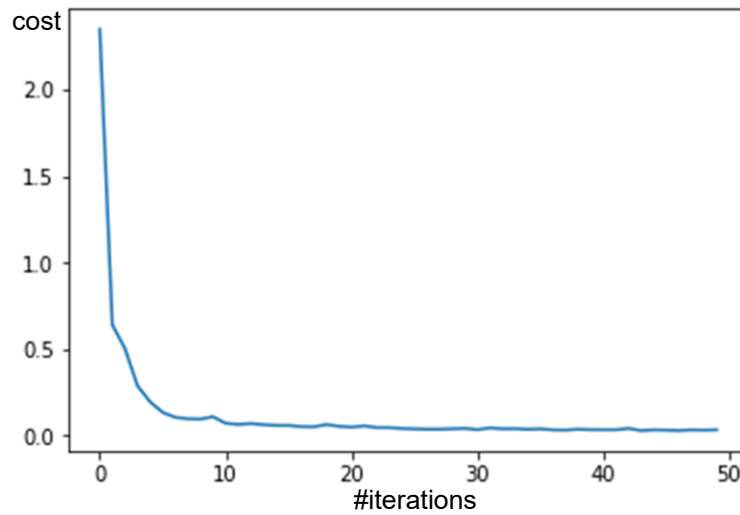
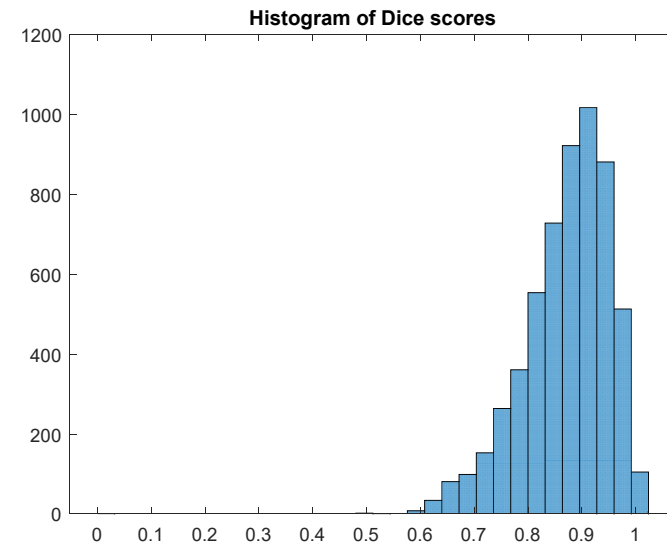


**Figure 4** AIF detection performance on the test set. (a) cost vs. the number of iterations for a typical training session, (b) histogram of three-class detection for all test cases, showing majority of cases have high dice scores.



(a) Cost vs. number of iterations



(b) Histogram of Dice ratios

**Figure 5** Examples of AIF detection with different level of performance. Cases with lower score still located the LV blood pool successfully.

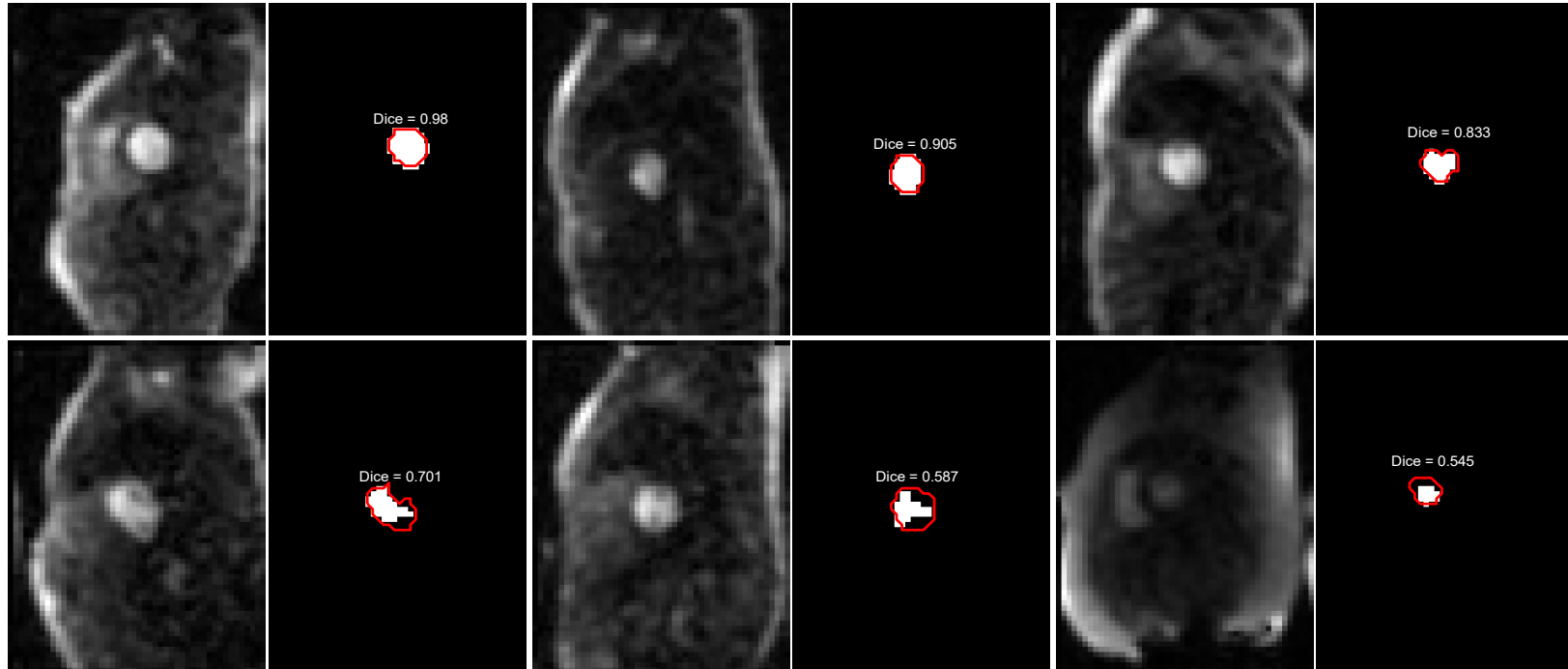


**Figure 6** Bland Altman plots for parameters derived from AIF signal curve comparing manually labelled vs. neural net based segmentation approaches.

